

Structure of electroweak dumbbells

Teerthal Patel, Tanmay Vachaspati

**Physics Department, Arizona State University, Tempe, Arizona 85287, USA.*

We analyze the magnetic field of electroweak dumbbells. While the magnetic field of the untwisted dumbbell is given by the usual dipole formula and falls off as $1/r^3$, dumbbells with twist have a novel twisted magnetic field that only falls off as $\cos\theta/r^2$ (in spherical coordinates). We comment on the relevance of twisted electroweak dumbbells for understanding the coherence of the magnetic field generated at the electroweak phase transition.

I. INTRODUCTION

The “electroweak dumbbell” consists of a magnetic monopole and an antimonopole of the standard electroweak model connected by a string made of Z -magnetic field [1, 2]. The existence of such non-perturbative field configurations in the electroweak model is of great interest as they would provide the first evidence for (confined) magnetic monopoles. In a cosmological context, dumbbells can source large-scale magnetic fields which can seed galactic magnetic fields and play an important role in the propagation of cosmic rays [3].

Generally electroweak dumbbells are viewed as magnetic dipoles with the usual dipolar $1/r^3$ fall off of the magnetic field strength with distance r from the dipole, but the situation in the electroweak case is richer. There is a one-parameter set of electroweak dumbbell configurations, all describing a confined monopole-antimonopole pair but with additional structure called the “twist”. Such twisted dumbbells are closely related to the electroweak sphaleron as they also carry Chern-Simons number [4].

In the paper we investigate the structure of electroweak dumbbells using “constrained relaxation”. We start with a field configuration that contains a monopole and an antimonopole with a relative twist. The fields are then relaxed subject to the constraint that the orientation of the Higgs field is held fixed throughout the spatial volume, and this automatically fixes the monopole-antimonopole positions and the twist.

For zero twist, we find the expected dipolar structure of the magnetic field of the system. The results for non-zero twist are more unexpected. The magnetic field lines do not connect the monopole to the antimonopole; instead the field lines stretch to infinity, tending to pull the monopole and antimonopole away from each other. At large distances from the dumbbell, the magnetic field strength has a $\cos\theta/r^2$ behavior. The magnetic field of a twisted dumbbell also has an azimuthal component, resembling the twisted field pointed out for an electroweak sphaleron in Ref. [5, 6].

We begin our analysis by describing the model and our initial configuration of fields in Sec. II. The numerical relaxation scheme is described in Sec. III. We define the electromagnetic field in Sec. IV and derive the magnetic field configuration for the initial unrelaxed config-

uration. The results of our constrained relaxation are given in Sec. V. We discuss consequences of our findings in Sec. VI.

II. MODEL

A. Electroweak model

The Lagrangian for the bosonic sector of the electroweak theory is given by

$$\mathcal{L} = -\frac{1}{4}W_{\mu\nu}^a W^{a\mu\nu} - \frac{1}{4}Y_{\mu\nu} Y^{\mu\nu} + |D_\mu\Phi|^2 - \lambda(|\Phi|^2 - \eta^2)^2, \quad (1)$$

where

$$D_\mu \equiv \partial_\mu - \frac{i}{2}g\sigma^a W_\mu^a - \frac{i}{2}g'Y_\mu. \quad (2)$$

Here, Φ is the Higgs doublet, W_μ^a are the SU(2)-valued gauge fields with $a = 1, 2, 3$ and, Y_μ is the U(1) hypercharge gauge field. In addition, σ^a are the Pauli spin matrices with $\text{Tr}(\sigma^a\sigma^b) = 2\delta_{ab}$, and the experimentally measured values of the parameters that we adopt from [7] are $g = 0.65$, $\sin^2\theta_w = 0.22$, $g' = g \tan\theta_w$, $\lambda = 0.129$ and $\eta = 174\text{GeV}$.

We adopt the temporal gauge for convenience in numerical implementation, with $W_0^a = B_0 = 0$. The Euler-Lagrange equations of motion for the model are given by

$$D_\mu D^\mu\Phi + 2\lambda(|\Phi|^2 - \eta^2)\Phi = 0 \quad (3)$$

$$\partial_\mu Y^{\mu\nu} = g' \text{Im}[\Phi^\dagger(D^\nu\Phi)] \quad (4)$$

$$\partial_\mu W^{a\mu\nu} + g\epsilon^{abc}W_\mu^b W^{c\mu\nu} = g \text{Im}[\Phi^\dagger\sigma^a(D^\nu\Phi)] \quad (5)$$

where the gauge field strengths are given by

$$W_{\mu\nu}^a = \partial_\mu W_\nu^a - \partial_\nu W_\mu^a + g\epsilon^{abc}W_\mu^b W_\nu^c \quad (6)$$

$$Y_{\mu\nu} = \partial_\mu Y_\nu - \partial_\nu Y_\mu. \quad (7)$$

Electroweak symmetry breaking results in three massive gauge fields, the two charged W bosons and Z_μ , and one massless gauge field, A_μ , that is the electromagnetic gauge field. We define

$$Z_\mu \equiv \cos\theta_w n^a W_\mu^a + \sin\theta_w Y_\mu, \quad (8)$$

$$A_\mu \equiv -\sin\theta_w n^a W_\mu^a + \cos\theta_w Y_\mu, \quad (9)$$

where

$$n^a \equiv \frac{\Phi^\dagger \sigma^a \Phi}{|\Phi|^2}. \quad (10)$$

The weak mixing angle, θ_w is given by $\tan \theta_w = g'/g$, the electric charge is given by $e = g_z \sin \theta_w \cos \theta_w$ and the Z coupling is defined as $g_z \equiv \sqrt{g^2 + g'^2}$. The Higgs, Z and W boson masses are given by $m_H \equiv 2\sqrt{\lambda}\eta = 125$ GeV, $m_Z \equiv g_z \eta / \sqrt{2} = 80$ GeV and $m_W \equiv g\eta / \sqrt{2} = 91$ GeV, respectively.

B. Initial field configuration

Here we setup a field configuration that describe the dumbbell. This configuration will become our starting

$$\hat{\Phi}_{m\bar{m}}(\gamma) = \begin{pmatrix} \sin(\theta_m/2) \sin(\theta_{\bar{m}}/2) e^{i\gamma} + \cos(\theta_m/2) \cos(\theta_{\bar{m}}/2) \\ \sin(\theta_m/2) \cos(\theta_{\bar{m}}/2) e^{i\phi} - \cos(\theta_m/2) \sin(\theta_{\bar{m}}/2) e^{i(\phi-\gamma)} \end{pmatrix}, \quad (12)$$

where the monopole and antimonopole are located along the z -axis, as illustrated in Fig. 1, and we have included a ‘‘twist’’ angle γ . In the limit $\theta_{\bar{m}} \rightarrow 0$, (12), one recovers the monopole configuration and, in the limit $\theta_m \rightarrow \pi$, one recovers the antimonopole configuration in (12) but with a twist given by γ . The effect of the relative twist γ is more evident from the vector (10) associated with the Higgs field. This is visualized in Cartesian space in Figs. 2 and 3. Here, we see the projection $\hat{n} - (\hat{n} \cdot \hat{j})\hat{j}$ of the vector in the xz -plane for extreme values of twists $\gamma = 0, \pi$.

The gauge field configurations are obtained by setting the covariant derivative of the Higgs field to vanish in the symmetry broken regions. This procedure does not fix the gauge fields completely as it allows for an arbitrary electromagnetic gauge field (since the generator of the electromagnetic group annihilates Φ). The electromagnetic gauge field is defined as,

$$A_\mu \equiv -\sin \theta_w \hat{n}^a W_\mu^a + \cos \theta_w Y_\mu. \quad (13)$$

We completely fix the form of the gauge fields by requiring that $A_\mu = 0$. The gauge fields are then given by,

$$gW_\mu^a = -\epsilon^{abc} n^b \partial_\mu n^c - i \cos^2 \theta_w n^a (\hat{\Phi}^\dagger \partial_\mu \hat{\Phi} - \partial_\mu \hat{\Phi}^\dagger \hat{\Phi}) \quad (14)$$

$$g'Y_\mu = -i \sin^2 \theta_w (\hat{\Phi}^\dagger \partial_\mu \hat{\Phi} - \partial_\mu \hat{\Phi}^\dagger \hat{\Phi}) \quad (15)$$

To correctly account for the radial dependence of the Higgs field around the monopole-antimonopole pair, we attach radial profiles. The general monopole solution is given by

$$\Phi = h(r) \hat{\Phi}, \quad (16)$$

point for constrained numerical relaxation, a process in which the total energy reduces while the monopole and antimonopole are held fixed at their initial locations.

The angular distribution of the Higgs field for the monopole and antimonopole can be taken to be [1],

$$\hat{\Phi}_m = \begin{pmatrix} \cos(\theta_m/2) \\ \sin(\theta_m/2) e^{i\phi} \end{pmatrix}, \hat{\Phi}_{\bar{m}} = \begin{pmatrix} \sin(\theta_{\bar{m}}/2) \\ \cos(\theta_{\bar{m}}/2) e^{i\phi} \end{pmatrix}, \quad (11)$$

where the hat on Φ denotes that $|\hat{\Phi}| = 1$, (θ_m, ϕ) are spherical angular coordinates centered on the monopole, and $(\theta_{\bar{m}}, \phi)$ are corresponding angles centered on the anti-monopole, as shown in Fig. 1. The combined monopole-antimonopole ansatz for the Higgs field can be taken to be [4],

where $\hat{\Phi}$ are the normalized doublets in (11). Including profile functions in the ansatz, the initial monopole-antimonopole scalar field configuration is given by

$$\Phi_{m\bar{m}} = k(\vec{x}) h(r_m) h(r_{\bar{m}}) \hat{\Phi}_{m\bar{m}}, \quad (17)$$

where r_m and $r_{\bar{m}}$ are radial coordinates centered on the monopole and antimonopole, respectively, given by

$$r_m = |\vec{x} - \vec{x}_m|, \quad r_{\bar{m}} = |\vec{x} - \vec{x}_{\bar{m}}|, \quad (18)$$

where $\vec{x}_m = (0, 0, d)$ and $\vec{x}_{\bar{m}} = (0, 0, -d)$. While $h(r)$ represents the monopole profile function, $k(\vec{x})$ in (17) is the profile of the Z -string that connects the monopole and the antimonopole in the dumbbell.

Similar to (17), we include radial profiles for the gauge fields as

$$gW_\mu^a = l(\vec{r}) j(r_m) j(r_{\bar{m}}) [-\epsilon^{abc} n^b \partial_\mu n^c - i \cos^2 \theta_w n^a (\hat{\Phi}^\dagger \partial_\mu \hat{\Phi} - \partial_\mu \hat{\Phi}^\dagger \hat{\Phi})] \quad (19)$$

$$g'Y_\mu = l(\vec{r}) j(r_m) j(r_{\bar{m}}) [-i \sin^2 \theta_w (\hat{\Phi}^\dagger \partial_\mu \hat{\Phi} - \partial_\mu \hat{\Phi}^\dagger \hat{\Phi})] \quad (20)$$

Now that we have set up a field configuration that describes the initial dumbbell in Eqs. (17), (19) and (20), we will perform a constrained numerical relaxation, a process in which the total energy reduces while the monopole and antimonopole are held fixed at their initial positions.

C. Profiles

The monopole profile functions are only known in closed form within the context of the Bogomolny-

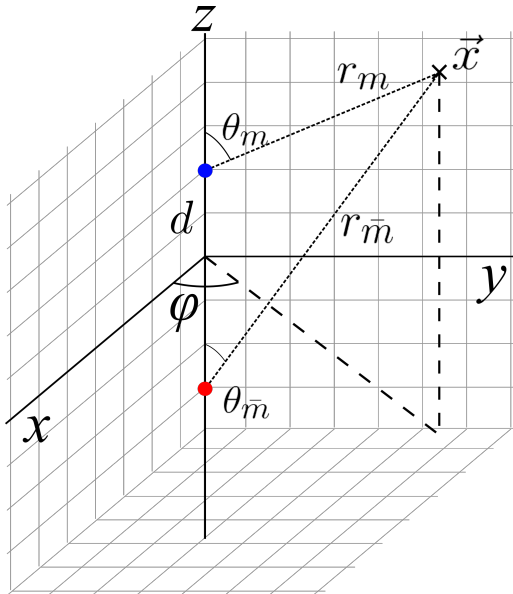


FIG. 1: A general vector \vec{x} in a Cartesian grid with the monopole and antimonopole centered polar angles, θ_m and $\theta_{\bar{m}}$, respectively.

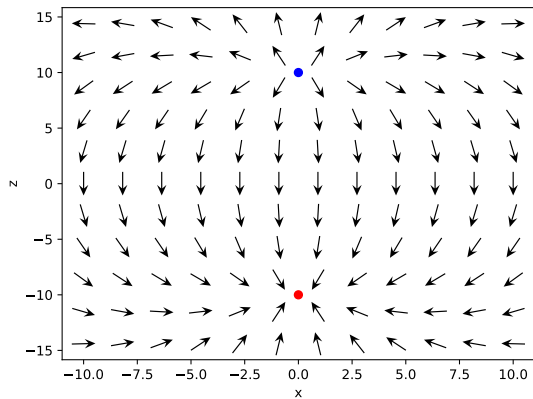


FIG. 2: The projection of the vector \hat{n} given by (10) for the ansatz (12) in the xz plane for $\gamma = 0$. The blue and red dots represent the monopole and antimonopole, respectively.

Prasad-Sommerfield (BPS) limit ($\lambda \rightarrow 0$) [8]. Numerical solutions for the general case have been outlined in [9]. A functional form that reduces to the BPS case is given by [10],

$$h(r) = \frac{1}{\tanh(\eta r)} - (1 + mr) \frac{e^{-mr}}{\eta r}, \quad (21)$$

$$j(r) = 1 - \frac{\eta r}{\sinh(\eta r)}, \quad (22)$$

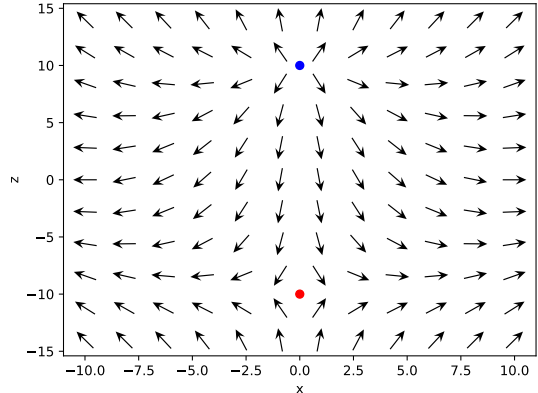


FIG. 3: The projection of the vector \hat{n} given by (10) for the ansatz (12) in the xz plane for $\gamma = \pi$. The blue and red dots represent the monopole and antimonopole, respectively.

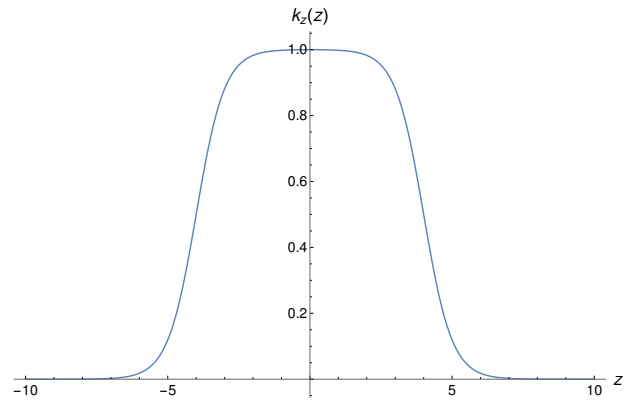


FIG. 4: The component $k_z(z)$ of the string profile $k(\vec{x})$, given by (24), as a function of z . The monopole and antimonopole are located at $z = \pm 4\eta^{-1}$, respectively.

where $m = 2\sqrt{\lambda}\eta$ is the scalar mass and r is the radial coordinate centered around the monopole. In our application, we use these radial profiles as initial guess functions for the monopole and the antimonopole.

The string profile functions have been studied in the context of the Abelian Higgs model, known as Nielsen-Olesen strings [11, 12]. The Nielsen-Olesen string profiles are not known analytically, but have been studied numerically. Our string profile guess functions $k(\vec{x})$ and $l(\vec{x})$ match the $\rho \rightarrow 0$ and $\rho \rightarrow \infty$ behavior of Nielsen-Olesen string solutions, where $\rho \equiv \sqrt{x^2 + y^2}$. However, unlike the Nielsen-Olesen case, we are dealing with a finite Z-string that joins the monopole-antimonopole pair. Therefore, our guess functions depend on \vec{x} and not just ρ , allowing the string profile function to terminate smoothly at the monopole and antimonopole. To this end, we define the string profile function by writing it as

$$k(\vec{x}) = 1 - k_\rho(\rho)k_z(z), \quad (23)$$

where k_z is the function that ensures that the Z-string

III. NUMERICAL RELAXATION

A. System of equations

The static equation of motion for Φ can be expanded as

$$\begin{aligned}
0 &= \partial_0^2 \Phi = D_i D_i \Phi - 2\lambda(|\Phi|^2 - \eta^2)^2 \Phi \\
&= \nabla^2 \Phi - i\frac{g}{2}\sigma^a W_i^a \partial_i \Phi - i\frac{g'}{2} Y_i \partial_i \Phi \\
&\quad - i\frac{g}{2}\sigma^a \Gamma_i^a \Phi - i\frac{g'}{2} \Xi_i \Phi^\alpha - i\frac{g}{2}\sigma^a W_i^a (D_i \Phi) \\
&\quad - i\frac{g'}{2} Y_i D_i \Phi - 2\lambda(|\Phi|^2 - \eta^2)^2 \Phi. \tag{26}
\end{aligned}$$

Here, we introduced the notation $\Gamma_i^a = \partial_i W_i^a$ and $\Xi_i = \partial_i Y_i$. Since we are computing the static configurations for the monopole-antimonopole pair, we set all time derivatives to be 0. Similarly, the static gauge field equations of motion lead to

$$\begin{aligned}
0 &= \nabla^2 W_i^a - \partial_i \Gamma_k^a - g\epsilon^{abc}(\partial_k W_i^b) W_k^c - g\epsilon^{abc} W_i^b \Gamma_k^c \\
&\quad - g\epsilon^{abc} W_k^b W_{ik}^c + g\text{Im}[\Phi^\dagger \sigma^a (D_i \Phi)] \tag{27} \\
0 &= \nabla^2 Y_i - \partial_i \Xi_k + g'\text{Im}[\Phi^\dagger \sigma^a (D_i \Phi)]. \tag{28}
\end{aligned}$$

The relaxation scheme entails that we fix the monopole-antimonopole positions when solving the system of equations (26)-(28). We implement this constraint by utilizing the gauge freedom in the model. We work in the gauge where the Higgs directions are chosen to be $\hat{\Phi}_{m\bar{m}}$ as given in (12). Since the positions of the monopole and antimonopole are determined by the orientation of the Higgs as discussed in Ref. [13], this fixes their positions for the entire relaxation process. Only the magnitude of the Higgs field $|\Phi|$ and the gauge fields, W_i^a and Y_i need to be relaxed to satisfy the equations of motion in (27) and (28). Thus instead of solving for the two components of the Higgs doublet, we solve for $|\Phi|$, where

$$|\Phi| = \frac{1}{2}(\hat{\Phi}^\dagger \Phi + \Phi^\dagger \hat{\Phi}).$$

The Laplacian of $|\Phi|$ can be expressed as

$$\begin{aligned}
\nabla^2 |\Phi| &= \frac{1}{2}[(\nabla^2 \hat{\Phi}^\dagger) \Phi + \hat{\Phi}^\dagger (\nabla^2 \Phi) \\
&\quad + (\nabla^2 \Phi^\dagger) \hat{\Phi} + \Phi^\dagger (\nabla^2 \hat{\Phi}) \\
&\quad + 4|\Phi| \partial_i \hat{\Phi}^\dagger \partial_i \hat{\Phi}] \tag{29}
\end{aligned}$$

where we have used

$$\partial_i \Phi = \partial_i |\Phi| \hat{\Phi} + |\Phi| \partial_i \hat{\Phi}. \tag{30}$$

and $\partial_i(\hat{\Phi}^\dagger \hat{\Phi}) = 0$. An equation of motion for $|\Phi|$ can thus be derived by using $\nabla^2 \Phi$ and $\nabla^2 \Phi^\dagger$ from (26) and, using (12) to obtain $\hat{\Phi}$ and its derivatives since, as explained above, $\hat{\Phi}$ is held fixed throughout the relaxation. Since, we are working in the temporal gauge, the equations for Γ_i^a and Ξ_i are trivial.

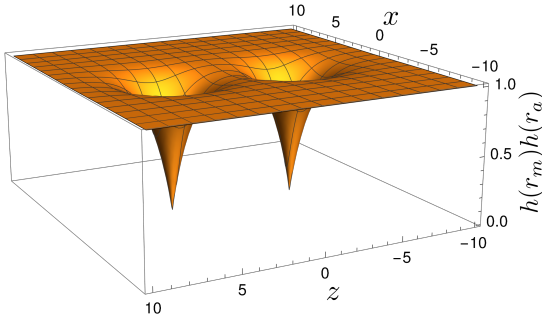


FIG. 5: The contour plots for the profile function $h(r_m)h(r_{\bar{m}})$ in the $y = 0$ plane. Here, the monopole and antimonopole are located at $z = \pm 4$, respectively.

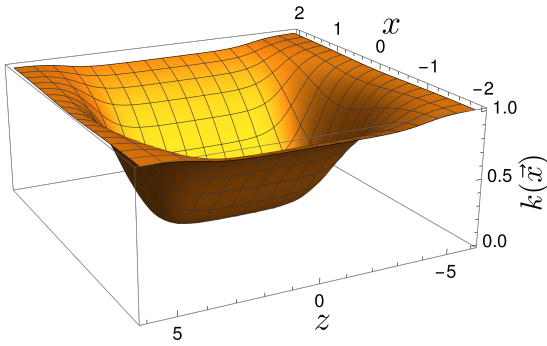


FIG. 6: The contour plots for the profile function $k(\vec{x})$ in the $y = 0$ plane. Here, the monopole and antimonopole are located at $z = \pm 4$, respectively.

terminates at the monopole and antimonopole, while k_ρ is the radial profile. These functions are taken to be

$$k_z(z) = \frac{\tanh(\eta(-z+d)) + \tanh(\eta(z+d))}{2 \tanh(\eta d)} \tag{24}$$

$$k_\rho(\rho) = \frac{\tanh(\eta(-\rho+\delta)) + \tanh(\eta(\rho+\delta))}{2 \tanh(\eta \delta)}. \tag{25}$$

where δ is the lattice spacing. k_z is illustrated in Fig. 4, and the total string profile, $k(\vec{x})$, is plotted in Figure 6.

One issue is that the profile $k(\vec{x})$ does not strictly vanish at the location of the string. This is not an issue for us because in our numerical work we place the string between lattice points and never have to evaluate the profiles exactly at the center of the string.

The initial Higgs and gauge fields are given by the configurations in Sec. II B and the guess profiles in Sec. II C. Furthermore, we evaluated the exact analytic first and second order derivatives of the Higgs and gauge fields for the initial configuration.

B. Relaxation algorithm

We relax the initial field configuration in a cubic lattice. At any given lattice point, the discretized system of equations is given by $\mathbf{E}_\alpha[f] = 0$, where $\mathbf{E}_\alpha[f]$ denote the discretized static equations for $f \in \{|\Phi|, W_i^a, Y_i\}$. The equations are of the wave equation type

$$\mathbf{E}_\alpha[f] = -\nabla^2 f_\alpha + S_\alpha[f] = 0 \quad (31)$$

where S_α denotes various other terms.

To illustrate the principle of numerical relaxation, consider the discretized second order spatial derivative,

$$\begin{aligned} \nabla^2 f_\alpha &\rightarrow -6\frac{f_\alpha}{\delta^2} + \frac{1}{\delta^2}[f_\alpha(i+1, j, k) + f_\alpha(i-1, j, k) \\ &\quad + f_\alpha(i, j+1, k) + f_\alpha(i, j-1, k) \\ &\quad + f_\alpha(i, j, k+1) + f_\alpha(i, j, k-1)] \\ &\equiv -6\frac{f_\alpha}{\delta^2} + \frac{\Delta_\alpha}{\delta^2} \end{aligned} \quad (32)$$

and so the equation of motion may be written as

$$f_\alpha(i, j, k) = \frac{\Delta_\alpha}{6} - \frac{\delta^2}{6} S_\alpha \quad (33)$$

which can also be written as,

$$f_\alpha(i, j, k) = \frac{\delta^2}{6} \mathbf{E}_\alpha[f_\beta] + f_\alpha(i, j, k). \quad (34)$$

The relaxation scheme is to take the left-hand side at the n^{th} iteration step and the right-hand side at the previous iteration step,

$$f_\alpha^{(n)}(i, j, k) = \frac{\delta^2}{6} \mathbf{E}_\alpha[f^{(n-1)}] + f_\alpha^{(n-1)}(i, j, k). \quad (35)$$

Numerically, we iterate over the lattice points in a linear order to update the field values. In our setup, the updated field values are made immediately available for computing the field values at the next lattice site in the computation. This is the Gauss-Seidel method and thus does not require an additional array to hold field values from the previous iteration. We continue iterating while the total energy of the configuration keeps decreasing. In the example stated above, we used first order central finite differences which results in the $1/6$ coefficient. In our numerical runs, we use sixth order finite central differences and then the coefficient is $6/49$.

C. Numerical setup

For most of our numerical runs, we use a 740^3 lattice with lattice spacing $\delta = 0.05 \eta^{-1}$. We work in units of η . Thus a unit of energy in our simulation corresponds to $\eta = 174$ GeV. The monopole and string radii are comparable to the inverse of the gauge boson masses, $m_W^{-1} = \sqrt{2} \eta^{-1} / g \approx 44 \delta$. Therefore there are about 44 lattice points that resolve the radius of the monopole and a similar number for the string.

The monopole and antimonopole are zeros of the Higgs field at their respective centers. In addition, the coordinates along which the Z-string is centered are also zeros of the Higgs field. These could lead to artificial numerical singularities and so, we offset the center of the monopole and antimonopole away from the z -axis in the xy plane; that is to say that the monopole and antimonopole are at the coordinates $x = y = \delta/2, z = \pm(d + \delta/2)$. This also implies that the Z-string lies parallel to the z -axis, along $x = y = \delta/2$. As the algorithm iterates over the lattice, the system undergoes relaxation and slowly approaches the desired asymptotic solution with the changes becoming infinitesimal, as the number of iterations performed increases. Since this can prove to be impractical, we introduced an additional constraint that the iterations are stopped once the consecutive fractional difference of the total energy drops below a certain threshold. This threshold was taken to be 10^{-6} . Note that the number of total iterations required to reach a satisfactory asymptotic scaling depends on both simulation parameters, like the lattice size and spacing, as well as model parameters, such as separation and twist. We run our algorithm for a range of separations and twists. For the set of tested parameters, the number of iterations performed ranges between $\sim 20000 - 70000$.

IV. MAGNETIC FIELD

We adopt the definition for the electromagnetic field strength tensor in the symmetry broken phase ($|\Phi| = \eta$) [14, 15],

$$\begin{aligned} A_{\mu\nu} &\equiv -\sin \theta_w \hat{n}^a W_{\mu\nu}^a + \cos \theta_w Y_{\mu\nu} \\ &\quad - i \frac{2 \sin \theta_w}{g\eta^2} (D_\mu \Phi^\dagger D_\nu \Phi - D_\nu \Phi^\dagger D_\mu \Phi) \\ &= \partial_\mu A_\nu - \partial_\nu A_\mu \\ &\quad - i \frac{2 \sin \theta_w}{g\eta^2} (\partial_\mu \Phi^\dagger \partial_\nu \Phi - \partial_\nu \Phi^\dagger \partial_\mu \Phi). \end{aligned} \quad (36)$$

This definition implies the presence of non-zero electromagnetic fields for $A_\mu = 0$ due to the Higgs gradient term. In the unitary gauge, the Higgs gradient term vanishes and one recovers the standard expression for the Maxwellian electromagnetic fields.

We now obtain analytic expressions for the magnetic field of the unrelaxed electroweak dumbbell for arbitrary twist. The relaxation procedure will change the detailed

features of the magnetic field but still preserves the qualitative features of the unrelaxed configuration as we will see in Sec. V.

Eqs. (19) and (20) ensure that $A_\mu = 0$ and it is only necessary to evaluate the last term in (36). The definition of $A_{\mu\nu}$ assumes that electroweak symmetry is broken and the expression in (36) applies in regions where $|\Phi| \approx \eta$. Hence we can replace Φ by $\Phi_{m\bar{m}}$ of (12) and write,

$$\partial_i \Phi \equiv A \partial_i \theta_m + B \partial_i \theta_{\bar{m}} + C \partial_i \phi \quad (37)$$

where A , B and C are derivatives of Φ with respect to θ_m , $\theta_{\bar{m}}$ and ϕ respectively. Then

$$\begin{aligned} \partial_{[i} \Phi^\dagger \partial_{j]} \Phi &= (A^\dagger B - B^\dagger A) \partial_{[i} \theta_m \partial_{j]} \theta_{\bar{m}} \\ &+ (A^\dagger C - C^\dagger A) \partial_{[i} \theta_m \partial_{j]} \phi \\ &+ (B^\dagger C - C^\dagger B) \partial_{[i} \theta_{\bar{m}} \partial_{j]} \phi \end{aligned} \quad (38)$$

and the square brackets in the indices denote antisymmetrization.

From Fig. 1 we see,

$$\tan \theta_m = \frac{\rho}{z-d}, \quad \tan \theta_{\bar{m}} = \frac{\rho}{z+d}. \quad (39)$$

where ρ is the cylindrical radial coordinate. Therefore, after some algebra,

$$\partial_{[i} \theta_m \partial_{j]} \theta_{\bar{m}} = \frac{2d\rho}{r_m^2 r_{\bar{m}}^2} \partial_{[i} \rho \partial_{j]} z \quad (40)$$

$$\partial_{[i} \theta_m \partial_{j]} \phi = \frac{1}{r_m^2} [(z-d) \partial_{[i} \rho \partial_{j]} \phi - \rho \partial_{[i} z \partial_{j]} \phi] \quad (41)$$

$$\partial_{[i} \theta_{\bar{m}} \partial_{j]} \phi = \frac{1}{r_{\bar{m}}^2} [(z+d) \partial_{[i} \rho \partial_{j]} \phi - \rho \partial_{[i} z \partial_{j]} \phi] \quad (42)$$

Then from (36) we get the (cylindrical) components of the magnetic field,

$$B_\rho = -i\kappa \left[\frac{A^\dagger C - C^\dagger A}{r_m^2} + \frac{B^\dagger C - C^\dagger B}{r_{\bar{m}}^2} \right] \quad (43)$$

$$B_\phi = i\kappa \frac{2d\rho}{r_m^2 r_{\bar{m}}^2} (A^\dagger B - B^\dagger A) \quad (44)$$

$$\begin{aligned} B_z &= -i\frac{\kappa}{\rho} \left[(z-d) \frac{A^\dagger C - C^\dagger A}{r_m^2} \right. \\ &\quad \left. + (z+d) \frac{B^\dagger C - C^\dagger B}{r_{\bar{m}}^2} \right] \end{aligned} \quad (45)$$

with $\kappa \equiv 2 \sin \theta_w / g$.

The factors with the doublets A , B and C can be evaluated using derivatives of (12) with respect to θ_m , $\theta_{\bar{m}}$ and ϕ . The calculation simplifies if we write

$$\Phi = \sin(\theta_m/2) e^{i\gamma} \Phi_1 + \cos(\theta_m/2) \Phi_2 \quad (46)$$

where

$$\Phi_1 = \begin{pmatrix} \sin(\theta_{\bar{m}}/2) \\ \cos(\theta_{\bar{m}}/2) e^{i(\phi-\gamma)} \end{pmatrix}, \quad (47)$$

$$\Phi_2 = \begin{pmatrix} \cos(\theta_{\bar{m}}/2) \\ -\sin(\theta_{\bar{m}}/2) e^{i(\phi-\gamma)} \end{pmatrix} \quad (48)$$

with the properties $|\Phi_1| = 1 = |\Phi_2|$, $\Phi_1^\dagger \Phi_2 = 0$, $\Phi_1 = -2\partial_{\theta_m} \Phi_2$, and $\Phi_2 = 2\partial_{\theta_m} \Phi_1$. This gives

$$A^\dagger B - B^\dagger A = \frac{i}{2} \sin \gamma \cos \theta_m.$$

Similar calculations give

$$A^\dagger C - C^\dagger A = \frac{i}{2} [\sin \theta_m \cos \theta_{\bar{m}} - \cos \gamma \cos \theta_m \sin \theta_{\bar{m}}],$$

$$B^\dagger C - C^\dagger B = \frac{i}{2} [\cos \theta_m \sin \theta_{\bar{m}} - \cos \gamma \sin \theta_m \cos \theta_{\bar{m}}],$$

These expressions can now be inserted in (43), (44) and (45). The resulting expressions are not transparent and we shall focus on a few interesting features.

First of all consider the magnetic field twist given by B_ϕ ,

$$B_\phi = -\kappa d \sin \gamma \frac{\rho}{r_m^2 r_{\bar{m}}^2} \cos \theta_m \quad (49)$$

Note that the twisting is not symmetric in θ_m and $\theta_{\bar{m}}$. For example, B_ϕ vanishes for $\theta_m = \pi/2$ but not when $\theta_{\bar{m}} = \pi/2$. This is a feature stemming from our choice of the unrelaxed field. Upon relaxation the twist gets redistributed as in apparent in Sec. V where we plot the magnetic field in the $\theta_m = \pi/2$ plane. Also note that the twisting reverses direction under $\gamma \rightarrow -\gamma$.

Far from the dumbbell $r_m \approx r_{\bar{m}} \approx r$, $\theta_m \approx \theta_{\bar{m}} \approx \theta$, and $\rho = r \sin \theta$. Then

$$B_\phi = -\kappa d \sin \gamma \frac{\sin \theta \cos \theta}{r^3} \quad (50)$$

Hence the azimuthal field is non-vanishing only for $\gamma \neq 0$, falls off as $1/r^3$, and the twisting is of opposite signs for $\cos \theta > 0$ and $\cos \theta < 0$.

Next we consider the magnetic field in the $z = 0$ plane. Then we have $r_m = r_{\bar{m}} = \rho$ and $\theta_m + \theta_{\bar{m}} = \pi$. This gives us

$$B_\rho(z=0) = \frac{\kappa}{2\rho^2} (1 - \cos \gamma) \sin(\theta_m + \theta_{\bar{m}}) = 0 \quad (51)$$

$$B_z(z=0) = \frac{\kappa d}{2\rho^3} \sin(2\theta_m) (1 + \cos \gamma). \quad (52)$$

Hence for maximal twist angle, $\gamma = \pi$, the magnetic field on the $z = 0$ plane vanishes.

Finally we consider the asymptotic magnetic field. We have already calculated the azimuthal component in (50). For the other components, note that once again $r_m \approx r_{\bar{m}} \approx r$, $\theta_m \approx \theta_{\bar{m}} \approx \theta$ and so

$$B_\rho|_{r \gg d} = \kappa (1 - \cos \gamma) \frac{\sin \theta \cos \theta}{r^2} \quad (53)$$

and

$$B_z|_{r \gg d} = \kappa(1 - \cos \gamma) \frac{\cos^2 \theta}{r^2} \quad (54)$$

Note that the magnetic field of the twisted dumbbells ($\gamma \neq 0$) falls off as $1/r^2$, instead of the dipolar $1/r^3$.

Some more insight is gained by calculating the spherical radial component of the magnetic field in the asymptotic region. The radial component is given by

$$B_r = B_\rho \sin \theta + B_z \cos \theta. \quad (55)$$

Using (53) and (54) we get

$$B_r|_{r \gg d} = \kappa(1 - \cos \gamma) \frac{\cos \theta}{r^2}. \quad (56)$$

Therefore the radial field has the structure of a *monopole's* magnetic field that has been squeezed into the angular range $0 \leq \theta \leq \pi/2$, and an *antimonopole's* magnetic field squeezed in the angular range $\pi/2 < \theta < \pi$. The magnetic field vanishes at $\theta = \pi/2$. The long range magnetic field of a twisted dumbbell has a $1/r^2$ fall off, like that of a monopole. Only in the untwisted ($\gamma = 0$) case does this monopole contribution vanish, and then the dipole $1/r^3$ term becomes the leading contribution.

Many of the qualitative features of the initial magnetic field persist even after relaxation as we now discuss.

V. RESULTS

As a check of our numerical relaxation scheme we have calculated energies of the electroweak Z-string [16] and the electroweak sphaleron. Our relaxation procedure on a three dimensional lattice gives the energy per unit length of the Z-string to be $1.023\pi\eta^2$. This is within 2% of the values previously calculated from numerical solutions of the radial differential equations [11, 12]. For the second check, we obtained the energy of the electroweak sphaleron by using the configuration in (12) with twist $\gamma = \pi$ and zero separation, *i.e.* $\theta_m = \theta_{\bar{m}}$. Then $\Phi_{m\bar{m}}$ has the configuration of the $SU(2)$ ($\theta_w = 0$) sphaleron. On relaxing the configuration, we find the sphaleron energy to be $2.00 \times 4\pi$ for $\lambda = 1/2$ and $\theta_w = 0$, which is within 1% of the result in [9].

In Fig. 7, we show the energies of electroweak dumbbell configurations for two different monopole-antimonopole separations, and a few different twists as a function of the number of iterations in our relaxation procedure. The solid lines are asymptotic fits that show convergence of the energies of the configurations. In Fig. 8 we show the energies of the relaxed electroweak dumbbells for twist angle $\gamma \in [0, \pi]$, and for a range of separations. At large separations, most of the energy is in the string and hence we see linear growth. At small separations the string is less important and monopole-antimonopole interactions become important. The flattening of the $\gamma = \pi$ curve

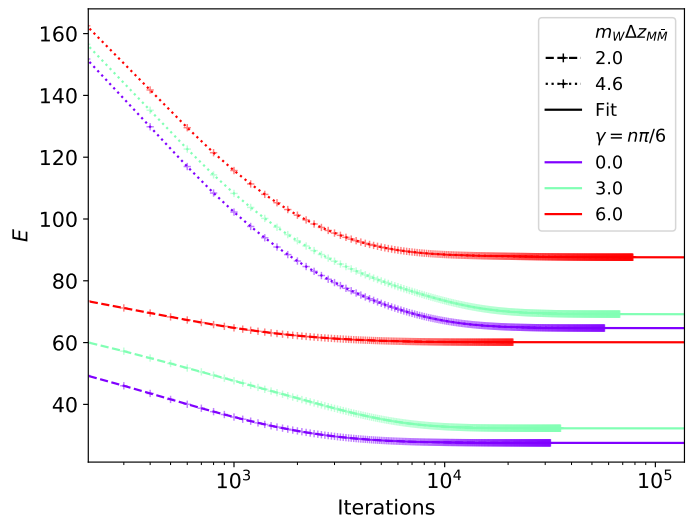


FIG. 7: The energy of the configuration as a function of the number of iterations for twist angle $n\pi/6$, $n = 0, 3, 6$. The different colors and line styles correspond to different values of n and monopole-antimonopole separation $\Delta z_{M\bar{M}}$, as indicated in the legends. The solid lines are asymptotic fits to the converged energies.

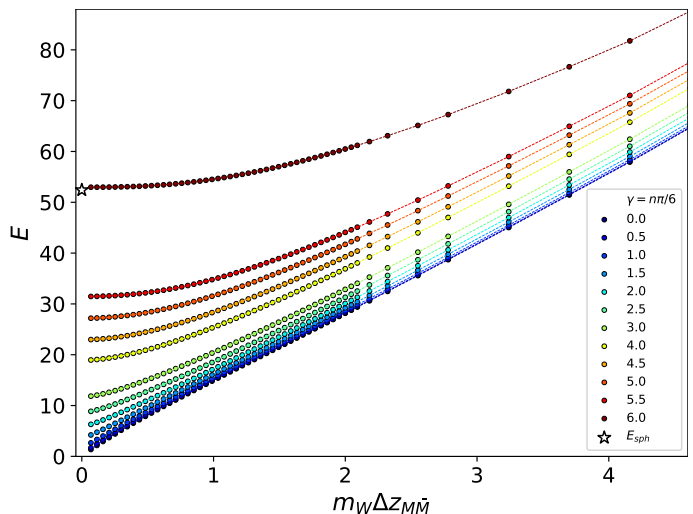


FIG. 8: The energy of electroweak dumbbells as a function of monopole-antimonopole separation for twist angle $\gamma = n\pi/6$ for various values of n as shown in the legend. The energies increase as we increase the twist. The star at minimal separation and $\gamma = \pi$ denotes the sphaleron.

at very small separations indicates the existence of an unstable solution, which is precisely the sphaleron.

In Fig. 9, we show contours of the magnitude of the relaxed Higgs field $|\Phi|$ in the xz -plane for twist π . There are no significant differences in features for different values of the twist γ .

To find the magnetic structure of the electroweak dumbbell we use the definition of the field strength in (36). This expression assumes $|\Phi| = \eta$ and hence is strictly valid only far from the dumbbell. However, we

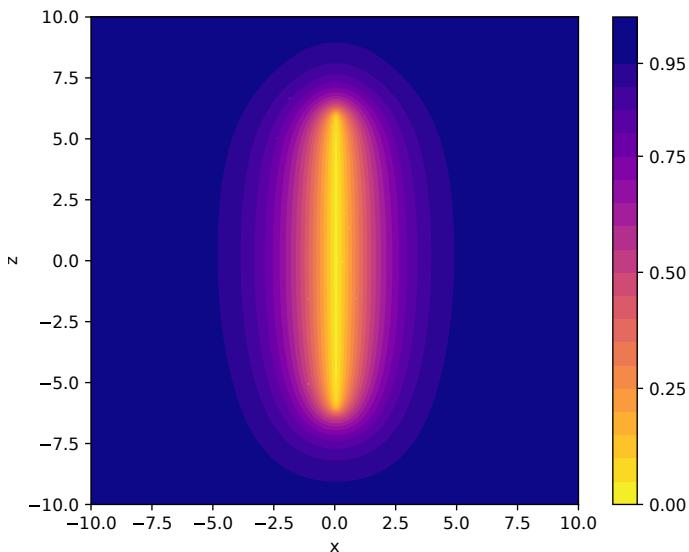


FIG. 9: Contours of the Higgs field magnitude $|\Phi|$ in units of η in the xz -plane after relaxation for $\gamma = \pi$ and monopole-antimonopole separation of $2d = 120\delta = 12\eta^{-1}$. The same contour for the $\gamma = 0$ case has very similar features.

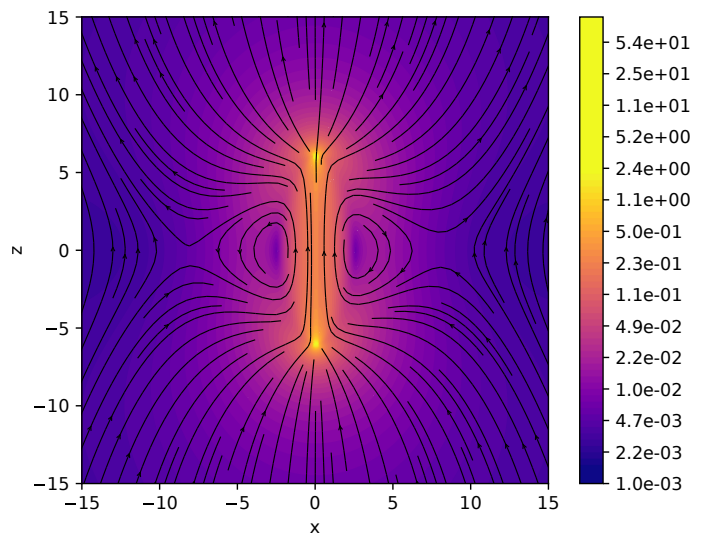


FIG. 11: Contours of the magnetic field magnitude $|B|$ (colors) in units of η^2 , and the projection of magnetic field lines in the xz -plane after relaxation for $\gamma = \pi$, and monopole-antimonopole separation $2d = 120\delta = 12\eta^{-1}$.

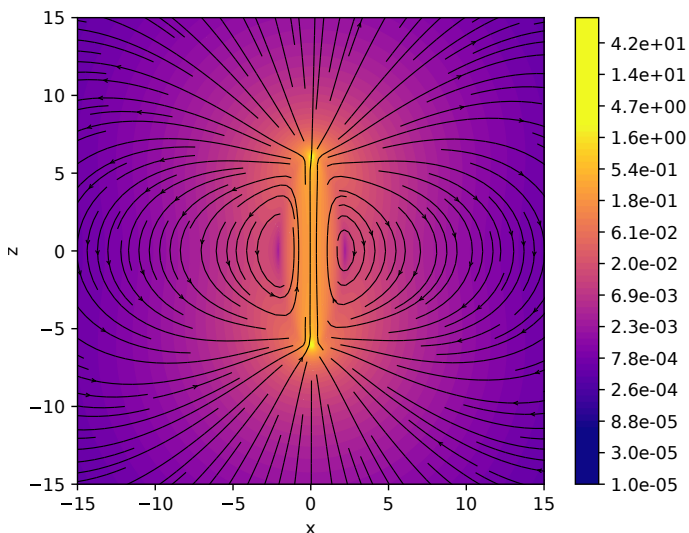


FIG. 10: Contours of the magnetic field magnitude $|B|$ (colors) in units of η^2 , and the projection of magnetic field lines in the xz -plane after relaxation for $\gamma = 0$, and monopole-antimonopole separation $2d = 120\delta = 12\eta^{-1}$.

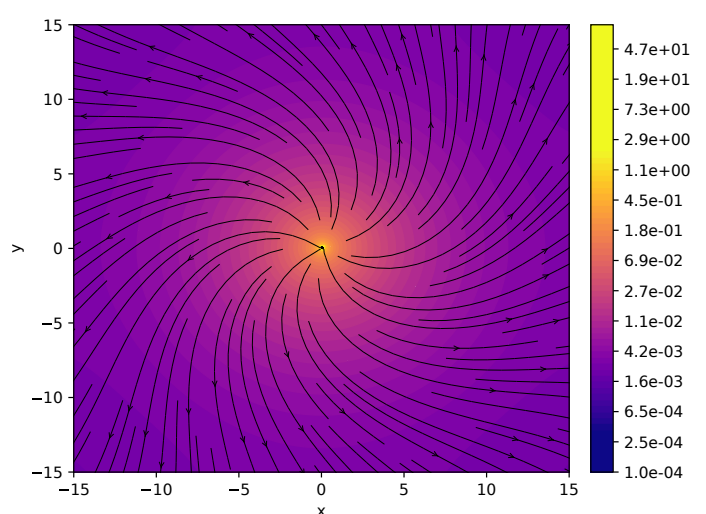


FIG. 12: Contour plots of the magnetic field magnitude $|B|$ (colors) in units of η^2 in the xy -plane containing the monopole ($z = d$), and the projection of magnetic field lines (black curves): $\vec{B} - (\vec{B} \cdot \hat{k})\hat{k}$, for $\gamma = \pi$, $2d = 12\eta^{-1}$.

will apply it to the entire volume; points where $\Phi = 0$ are avoided since the dumbbell zeros are situated between lattice points. In Fig. 10 we show the magnetic field strength (colors) and the magnetic field lines of an untwisted dumbbell.

The magnetic structure of the twisted ($\gamma = \pi$) dumbbell is shown in Fig. 12 and, in marked contrast to the untwisted case, the magnetic field lines flow away from the dumbbell. The structure agrees with the $\cos\theta/r^2$ expression given in (56). The magnetic field lines in this case tend to pull the monopole and antimonopole apart,

i.e. they provide a repulsive force between the monopole and antimonopole.

The field lines in Fig. 12 show the structure of the magnetic field projected on to the xz -plane: the field lines shown are given by the direction of $\vec{B} - (\vec{B} \cdot \hat{y})\hat{y}$ and suppresses the component out of the page (in the y -direction). In Fig. 12 we show the projected field lines in the $z = d$ plane. Here we clearly see the twist in the magnetic field lines first discussed in the context of the sphaleron in Ref. [5, 6].

VI. CONCLUSIONS AND DISCUSSION

We have developed a numerical technique to study the magnetic structure of electroweak dumbbells in which the positions of the monopole and antimonopole are held fixed. We have studied the constrained solution as a function of the monopole-antimonopole separation and the twist angle. As expected, the energy grows linearly with separation at large separations, while monopole-antimonopole interactions become important at small separations. For maximum twist, the dumbbell energy approaches the electroweak sphaleron energy as the separation goes to zero.

The magnetic field of the electroweak dumbbell at zero twist resembles that of an ordinary bar magnet. Then the magnetic field strength has the usual dipolar $1/r^3$ fall off at large distances. However the magnetic field in the case of non-zero twist has an unexpected distribution – the magnetic field lines emanating from the monopole, instead of terminating at the antimonopole, are directed towards spatial infinity and pull the monopole away from the antimonopole. The magnetic field strength at large distances has a $\cos\theta/r^2$ fall off. In addition, the magnetic field lines are twisted in the azimuthal direction.

For a general electroweak dumbbell formed during electroweak symmetry breaking, the twist angle will be non-zero and the magnetic field lines emanating from a monopole will terminate on an antimonopole of some

other dumbbell. After the dumbbells have annihilated, the remaining field lines will perform a random walk in three dimensions and will not close on themselves. This is likely to have consequences for the correlation length of magnetic fields leftover from the electroweak epoch [3]. The situation may be similar to that of cosmic strings in which most of the energy of the cosmic string network is in infinite strings and not in closed loops. We plan to examine this scenario in more detail in future work.

Another outcome of our work is in the context of Nambu's calculation of the lifetime of rotating electroweak dumbbells [1]. Our relaxation methods have provided the structure of the dumbbells which we can feed into an evolution code and study their lifetime as a function of energy and angular momentum.

Acknowledgments

This work was supported by the U.S. Department of Energy, Office of High Energy Physics, under Award No. DE-SC0019470. The authors acknowledge Research Computing at Arizona State University for providing access to high performance computing and storage resources on the Agave and Sol Supercomputer that have contributed to the research results reported within this paper.

-
- [1] Y. Nambu, Nucl. Phys. B **130**, 505 (1977).
 - [2] A. Achúcarro and T. Vachaspati, Phys. Rept. **327**, 347 (2000), hep-ph/9904229.
 - [3] T. Vachaspati, Rept. Prog. Phys. **84**, 074901 (2021), 2010.10525.
 - [4] T. Vachaspati and G. B. Field, Phys. Rev. Lett. **73**, 373 (1994), URL <https://link.aps.org/doi/10.1103/PhysRevLett.73.373>.
 - [5] M. Hindmarsh, in *1st International Conference on Strong and Electroweak Matter* (1994), hep-ph/9408241.
 - [6] M. Hindmarsh and M. James, Phys. Rev. D **49**, 6109 (1994), hep-ph/9307205.
 - [7] R. L. Workman and Others (Particle Data Group), PTEP **2022**, 083C01 (2022).
 - [8] M. K. Prasad and C. M. Sommerfield, Phys. Rev. Lett. **35**, 760 (1975), URL <https://link.aps.org/doi/10.1103/PhysRevLett.35.760>.
 - [9] N. S. Manton and P. Sutcliffe, *Topological solitons*, Cambridge Monographs on Mathematical Physics (Cambridge University Press, 2004), ISBN 978-0-521-04096-9, 978-0-521-83836-8, 978-0-511-20783-9.
 - [10] T. Vachaspati, Phys. Rev. D **93**, 045008 (2016), 1511.05095.
 - [11] H. B. Nielsen and P. Olesen, Nucl. Phys. B **61**, 45 (1973).
 - [12] A. Vilenkin and E. P. S. Shellard, *Cosmic Strings and Other Topological Defects* (Cambridge University Press, 2000), ISBN 978-0-521-65476-0.
 - [13] T. Patel and T. Vachaspati, JHEP **01**, 059 (2022), 2108.05357.
 - [14] G. 't Hooft, Nucl. Phys. B **79**, 276 (1974).
 - [15] T. Vachaspati, Phys. Lett. B **265**, 258 (1991).
 - [16] T. Vachaspati, Phys. Rev. Lett. **68**, 1977 (1992), URL <https://link.aps.org/doi/10.1103/PhysRevLett.68.1977>.